JOURNAL OF SOLID STATE CHEMISTRY 58, 389–397 (1985)

Structure and Microstructure of the Metastable B Phase ($NiAl_{10}O_{16}$)

II. An Electron Microscopic Investigation of the Microstructure

P. BASSOUL AND J. C. GILLES

Laboratoire de Chimie du Solide Minéral–UA 450, ESPCI 10 rue Vauquelin, 75231 Paris Cedex 05, France

Received May 25, 1984; in revised form December 26, 1984

The main features of the B phase microstructure of $NaAl_{10}O_{16}$ are analyzed by transmission electron microscopy. Strains introduced by nucleation and growth of this phase are canceled by the clustering of twin domains into three zones with four coaxial variants. Coherent and incoherent twin boundaries are analyzed. The former have a translation component and form triple junctions with nonperiodic antiphase boundaries. The latter are associated with planar faults. Regions with a high density of faults are frequently observed; the cation distribution in these faulted regions is interpreted as an intermediate order between the cation distributions of two twin variants. Boundaries between the 12 twin variants and the 8 translational variants leave unchanged the spinel domains of the periodic antiphase boundary structure of the B phase.

1. Introduction

The preparation and structure of the metastable B phase of $NaAl_{10}O_{16}$ have been described in Part I (*1*). Phase B has a periodic antiphase boundary (PAPB) structure based on $(100)_c$ planes of the spinel structure, with an antiphase vector $\mathbf{R} = \frac{1}{4}[1\bar{1}0]_c$. Phase B is prepared by annealing crystals of the ε_{Ni} metastable phase. ε_{Ni} also has a PAPB structure but based on $(310)_c$ spinel planes (*2*). Structure and twinning in the ε phases in $MgO–Ga_2O_3$ and $Li_2O–Al_2O_3$ systems have been studied previously (*3–5*). The transformation $\varepsilon_{Ni} \rightarrow$ B is not a simple one because of the small-scale twinning (12 twin variants) of these two phases. Part II is concerned with an electron microscopic investigation of the microstructure of the B phase. Boundary structure will be analyzed from the two points of view. Dealing first with the monoclinic distortion of the compact cubic oxygen array, invariant planes of this array common to the two twin lattices can be calculated when the distortion is described as an homogeneous lattice strain (*6*). Second, the cation distribution on boundaries is discussed; boundary structural models are constructed from electron microscopic data and from the B phase structural model given in Part I.

2. Experimental Methods

Thin foils suitable for transmission electron microscopy were prepared by mechanical polishing and the ion-thinning technique. They were coated on their two faces with amorphous carbon to prevent electrostatic charging of the sample. Bright and dark field images, as well as imaging of $(100)_m$ and $(010)_m$ planes with spacings $\simeq$7.9 Å, were performed on a JEOL 120 CX electron microscope equipped with a goniometric rotation-tilt stage.

0022-4596/85 $3.00

3. Twin Domain Morphology

In the following descriptions, lattice planes and directions are referred, as in Part I, to three unit cells:

(a) $\mathbf{a}_c$, $\mathbf{b}_c$, $\mathbf{c}_c$: cubic cell

(b) $\mathbf{a}'_c$, $\mathbf{b}'_c$, $\mathbf{c}'_c$: monoclinic pseudocubic cell used to describe the distortion

(c) $\mathbf{a}_m = \mathbf{a}'_c$, $\mathbf{b}_m = 2\mathbf{b}'_c$, $\mathbf{c}_m = \mathbf{c}'_c$, $\gamma_m = \gamma'_c$: B phase unit cell.

A. Twin Zones and Their Elastic Accommodation

Twins are clustered into three zones. Within each zone, four coaxial twin variants have a common binary axis along one of the $\langle 100 \rangle_c$ directions (Fig. 1). The relative orientations of these four twin variants are given in Fig. 2; they are denoted 1, 2, 3, 4 twin variants. We shall see in the next paragraph that twin domains are small and

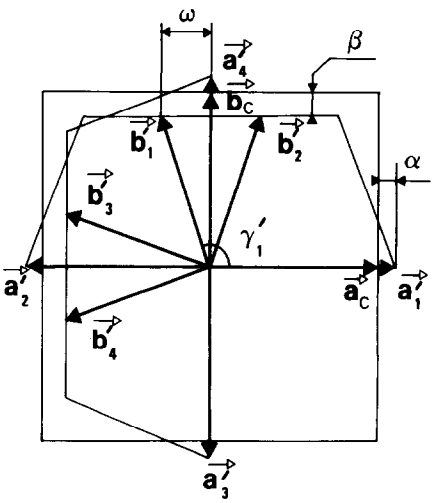

FIG. 2. Schematic drawing of the monoclinic distortion and of the orientation relationship between 1, 2, 3, 4 twin variants.

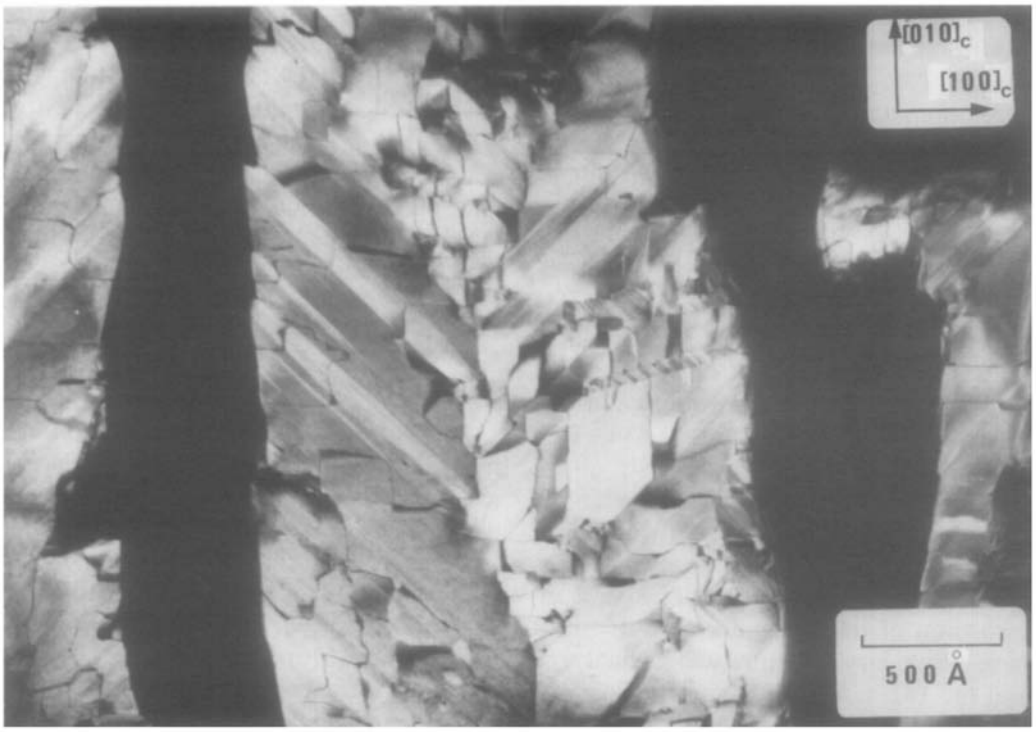

FIG. 1. Dark field micrograph showing a twin zone $\mathbf{g} = 100_1, \bar{1}00_2, 0\bar{2}0_3, 0\bar{2}0_4$.

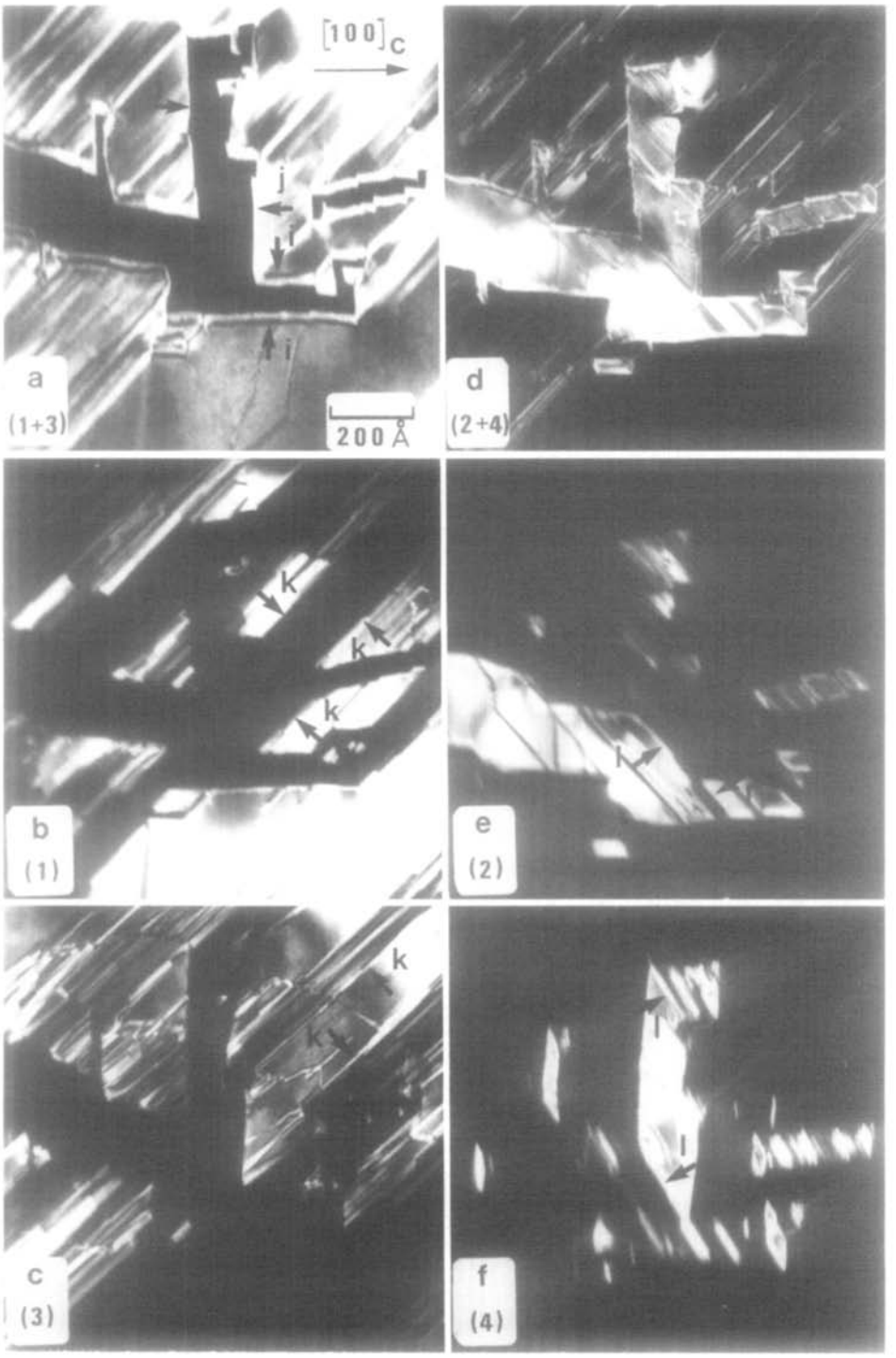

FIG. 3. Dark field micrographs in different reflections of four twin variants: (1) $\mathbf{g} = \bar{1}61_1, \bar{3}21_3$; (b) $\mathbf{g} = \bar{1}, 11, 1_1$; (c) $\mathbf{g} = \bar{5}31_3$; (d) $\mathbf{g} = 1, 10, 1_2, 521_4$; (e) $\mathbf{g} = 171_2$; (*f*) $\mathbf{g} = 311_4$. Twin boundary planes: (i) $(010)_c$; (j) $(100)_c$, (k) $(1\bar{1}0)_c$, (l) $(110)_c$.

quasi-homogeneously distributed into each zone. Thus, the strain associated with a twin zone could be taken as a macroscopic one and calculated by averaging the strain tensors of the four twin variants. The strain tensor of twin variant denoted 1, referring to the cubic cell, is calculated from the parameters of the monoclinic pseudocubic cell (*1*):

$$|e_{ij}|_1 = \begin{vmatrix} \alpha & \omega & 0 \\ 0 & \beta & 0 \\ 0 & 0 & 0 \end{vmatrix}$$

with

$$\alpha = \frac{a'_1}{a_c} - 1 = 34 \cdot 10^{-4}$$

$$\beta = \frac{b'_1 \sin \gamma'_1}{a_c} - 1 = -97 \cdot 10^{-4}$$

$$\omega = \frac{b'_1 \cos \gamma'_1}{a_c} = -190 \cdot 10^{-4}$$

Twin symmetry operations applied to $|e_{ij}|_1$ give the other twin variant strain tensors. The 1–2 and 3–4 twin variants have opposite shear strains. Averaging these four tensors gives a macroscopic strain for the $[001]_c$ twin zone, which corresponds to a very slight contraction ($\alpha + \beta)/2 \simeq -0.3\%$) along the $[100]_c$ and $[010]_c$ axes.

The previously studied ε phases (*3, 4*) have a similar distortion and display the same clustering as the B phase. This clustering permits shear strains to be canceled during precipitation of the ε phase in the spinel matrix. When ε_{Ni} is transformed into the B phase, the slight quadratic distortion of twin zones is unchanged. Thus there is no additional macroscopic strain if ε_{Ni} twin zones are transformed into B zones.

B. Twin Boundary Orientations

Identification of twin domains within each twin zone was made with a series of dark field images (Fig. 3). Two kinds of twin boundaries are observed.

The first are boundaries parallel to $(010)_c$ and $(100)_c$ planes (*i* and *j* planes of Fig. 3). Mirror symmetry in these planes relates twin variants 1 to 2 and 3 to 4. There is a perfect matching of lattices on these $(010)_m$ planes (Fig. 2) and these boundaries are coherent.

The second are boundaries parallel to the $(1\bar{1}0)_c$ and $(110)_c$ planes (*k* and *l* planes on Fig. 3). Mirror symmetry in these planes relate twin variants 1 to 3 and 2 to 4. In this case there is no good matching, since the $(\bar{1}20)_m$ planes of the two related twin variants are rotated by 0.35°. The constrast of $\{110\}_c$ twin boundaries is different from a simple plane interface contrast; many faults parallel to the boundary plane are observed (Fig. 3c). It can also be seen in Fig. 3 that there is no contact plane between twin domains related by $\pi/2$ rotations (1 to 4 and 2 to 3).

The structure of the two kinds of twin boundaries and their interaction with faults are discussed in the next paragraph.

4. Faults, Antiphase Boundaries, and Twin Boundary Structures

A. $(010)_m$ Twin Boundaries and Their Interaction with Antiphase Boundaries

The coherent $(010)_m$ twin boundaries are parallel to the PAPBs of the B phase structure. These boundaries frequently exhibit triple junctions with nonperiodic APBs parallel to $(100)_m$ (Figs. 4, 5). APBs are observed on dark field images obtained with satellites or additional reflections, but they are out of contrast on images made with fundamental spinel reflections. Therefore, APB vectors can only be the vectors of the spinel fcc cell that do not belong to the B cell (Fig. 6). The easiest way to introduce these APBs is to take a diamond mirror of the spinel structure as the twin symmetry operation. There are seven junctions giving

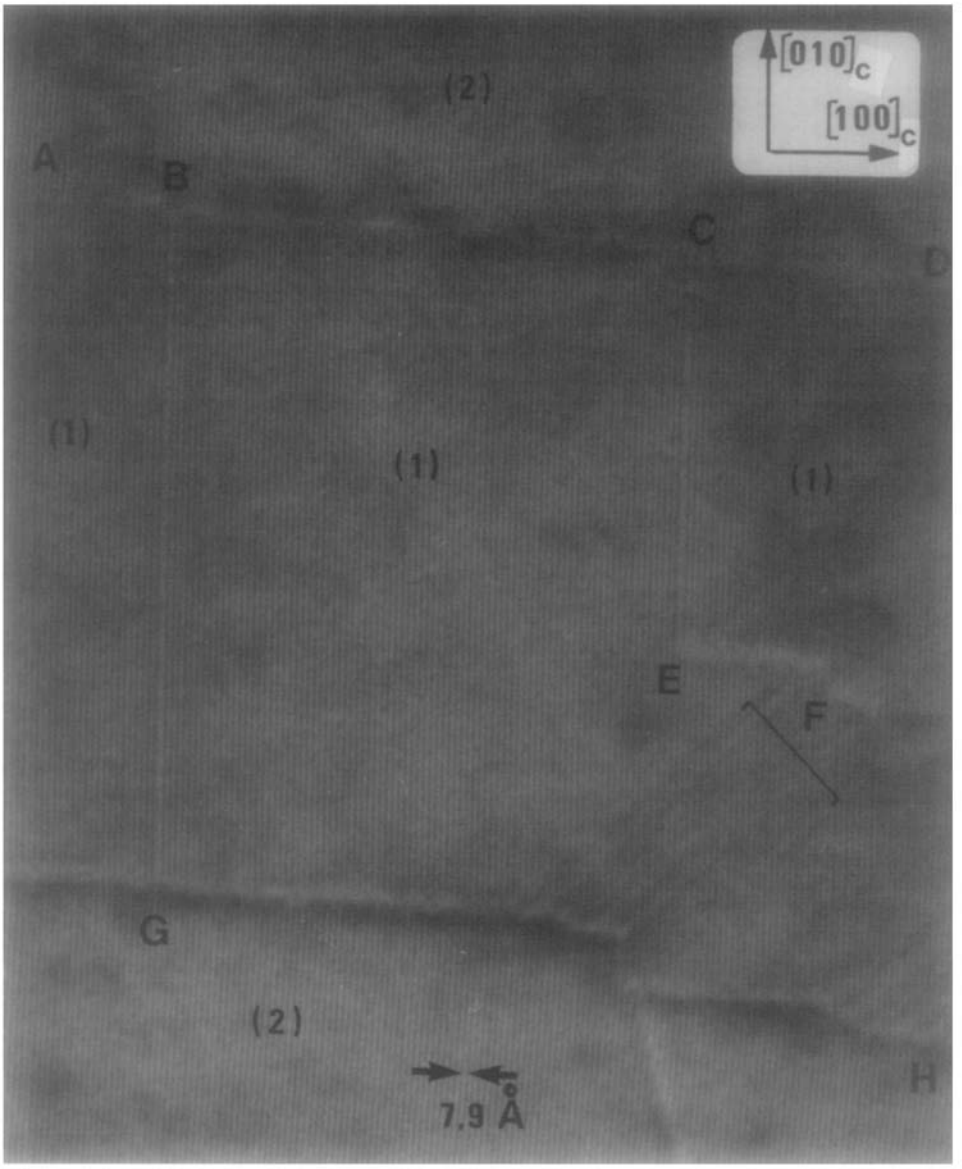

FIG. 4. Lattice fringes parallel to $(100)_1$ and $(100)_2$ planes with spacings d_{100_m}. AD and GH are $(010)_m$ twin boundaries. BG and CE are APBs. $(1\bar{2}0)_m$ planar faults appear in slight contrast on F region.

rise to seven APB vectors (Fig. 6), depending on the glide translation and on the relative positions of the diamond mirrors. Quite similar junctions have been observed previously by Van Tendeloo *et al.* (*7*). The junction in Fig. 5 is of type 3 or of type 7 as described in Fig. 6. The APB shifts $(100)_m$ and $(010)_m$ fringes. The twin boundary is displaced at the junction.

The $(010)_m$ twin boundaries and their associated APBs do not modify the cationic distribution in spinel domains of the B phase structure but they affect the PAPB arrangement near the boundary. Since cat-

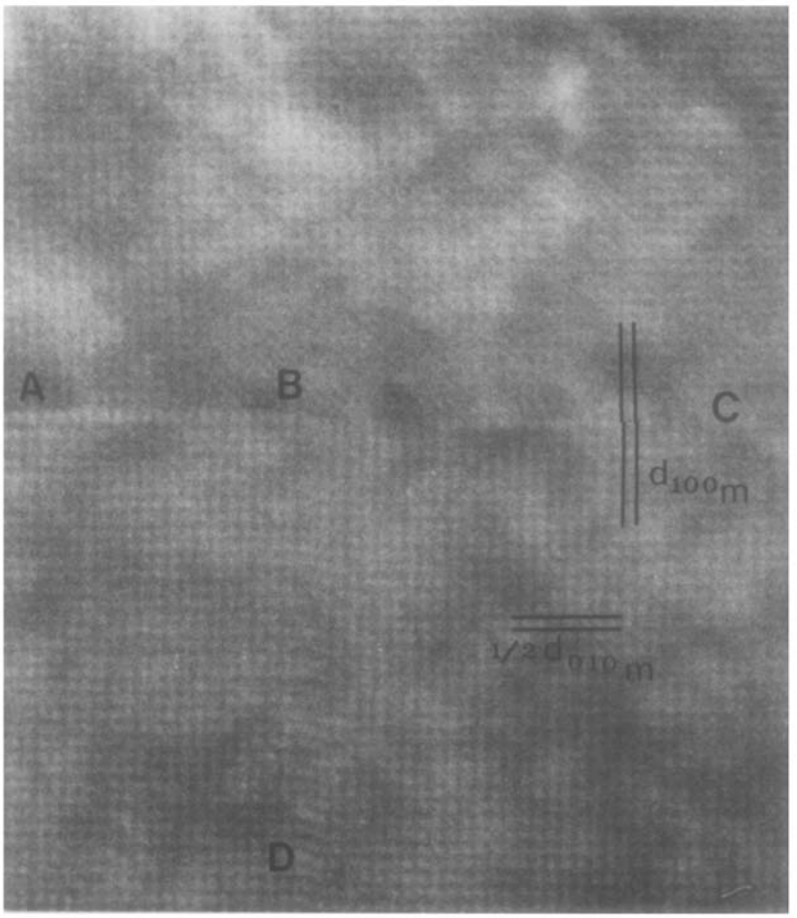

FIG. 5. Triple junction between two $(010)_m$ twin boundaries (AB and BC) and an APB (BD).

ion vacancies are ordered on PAPBs, the vacancy ratio near the twin boundary depends on the distance between the PAPBs that are related by the diamond mirror. $(010)_m$ boundary structural models can be built either with a slight increase, or with a slight decrease, of vacancy ratio. As a matter of fact, we have no sufficient experimental evidence to determine more precisely this twin boundary structure.

B. Planar Faults and Twin Boundaries on $(1\bar{2}0)_m$ *Planes*

Planar faults are observed in the vicinity of $\{110\}_c$ twin boundaries and also in each twin domain. They are frequently clustered (X regions in Fig. 7). These faults produce α fringes with two beam conditions (*8*). When considering $(h_m k_m l_m)$ reflexions, with $k_m = 2n + 1$, their contrast corresponds to π fringes. Furthermore, we can see in Fig. 4 (F region) that there is no shifting of $(100)_m$ lattice fringes when they cross the planar faults. These two observations are consistent with a fault vector $\mathbf{R} = [0\,\frac{1}{2}\,0]_m = [010]_c$.

The high density of $(1\bar{2}0)_m$ planar faults can explain the diffused lines observed along $[1\bar{2}0]^*_m$ directions in the X-ray and electron diffraction photographs (*9*). These lines pass through satellite reflections of

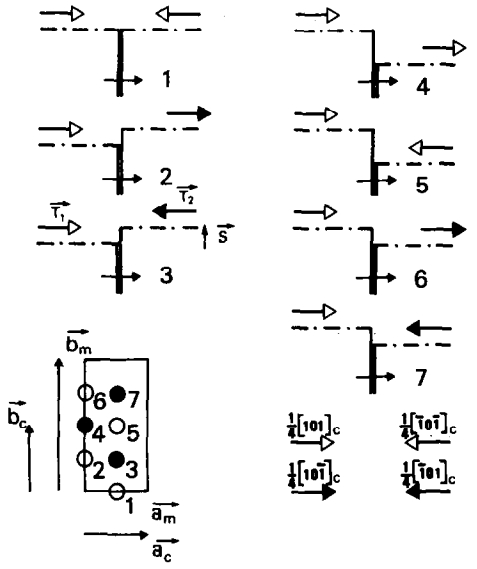

FIG. 6. Schematic drawings of triple junctions. Mixed lines correspond to the diamond glide planes of the spinel structure with their $\frac{1}{4}\langle 110\rangle_c$ translations. Double lines correpond to APB planes. The seven APB vectors are sketched on a $(001)_m$ projection of the B unit cell with heights: zero (●) and $c_m/2$ (○). The APB vector of a junction is equal to $\mathbf{T}_1 - \mathbf{T}_2 + 2\mathbf{S}$ (see junction 3 for example).

two twin variants related by a $(110)_c$ mirror plane (see Figs. 2 and 4 of Part I). $(1\bar{2}0)_m$ planar faults do not modify the composition of the B phase and produce the interesting property shown in the structural model of Fig. 8. Periodic $(1\bar{2}0)_m$ planar faults in the B structure do not determine a new structure but rather a twin domain related to the nonfaulted region by the glide mirror $(1\bar{2}0)_m$, $\frac{1}{4}[210]_m$. In this way $(1\bar{2}0)_m$ faults allow us to build a model of the $(1\bar{2}0)_m$ twin boundary structure. Nevertheless, planar fault contrasts observed near twin boundary planes (Fig. 3c) show that there is an intermediate region between twin domains where $(1\bar{2}0)_m$ periodic faults have irregular spacings. This faulted region displays a cation distribution different from the two twin domain regions. The distortion of the oxygen array in this region may improve the lattice matching of these incoherent boundaries.

5. Variant Number

In many phase transformations the number of variants and their symmetry relations can be predicted by a group-to-subgroup analysis between space groups of the parent and the transformed phases (*10*). When symmetry elements do not have the same orientation in each phase because of special topotactic relations, it is necessary to know the exact relative orientations of the two structures (*11*). In the case of the $\varepsilon_{Ni} \rightarrow$ B transformation there are no subgroup relations between the two structures, since their orientation symmetry groups are the same ($2/m$). Thus, the number of variants cannot be explained with geometric or topotactic relations. Nevertheless, one can assume an hypothetical parent phase. This parent phase does not have the spinel structure but rather a cubic structure with disordered cations in all octahedral and tetrahedral interstices of the oxygen array. The volume ratio between primitive cells of this structure and of the B structure gives 64 possible translation variants.

The more frequently observed APBs link eight translation variants only. The observed translation variants are those which give rise to translation and twin boundaries with the smallest interfacial energies. All these boundaries leave the spinel structure unchanged and therefore do not greatly increase the crystal electrostatic energy. In the cases of the other predicted variants, their boundaries will create many octahedral and tetrahedral sites sharing a face.

6. Conclusion

The metastable B phase ($NiAl_{10}O_{16}$) has a monoclinic periodic antiphase boundary structure built from the spinel structure. An electron microscopic investigation of twin and boundary relations allows us to explain the main features of the microstructure. The 12 twin variants are clustered into

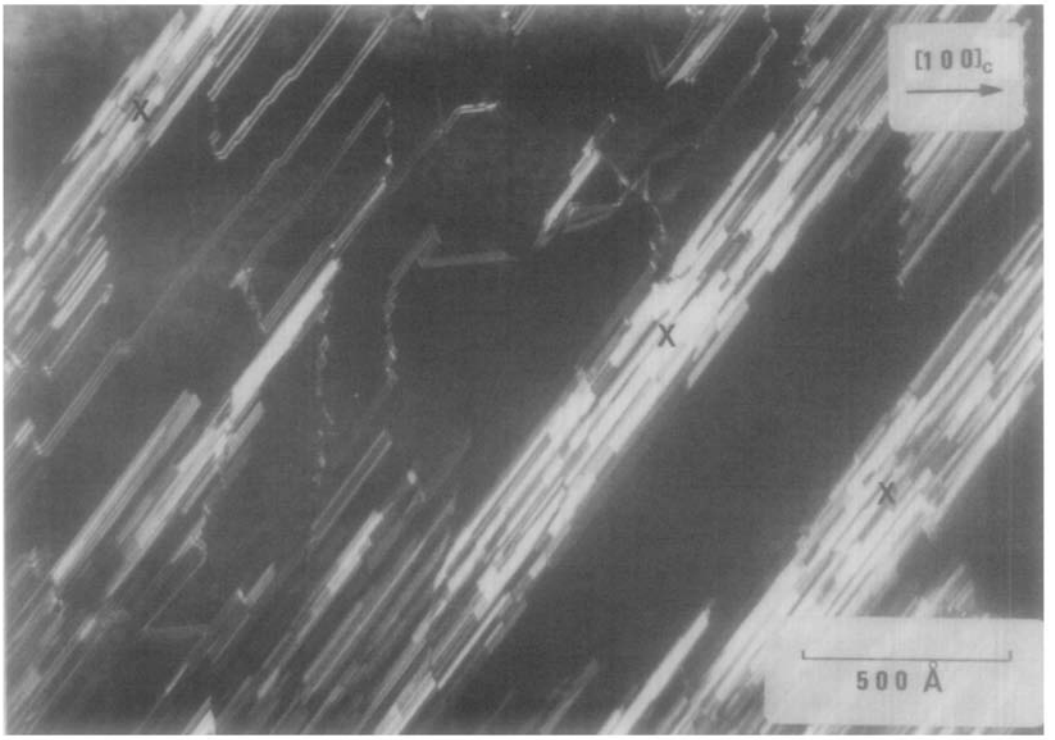

FIG. 7. Dark field image showing $(1\bar{2}0)_m$ planar faults ($\mathbf{g} = 191_1$). X regions have a high density of faults.

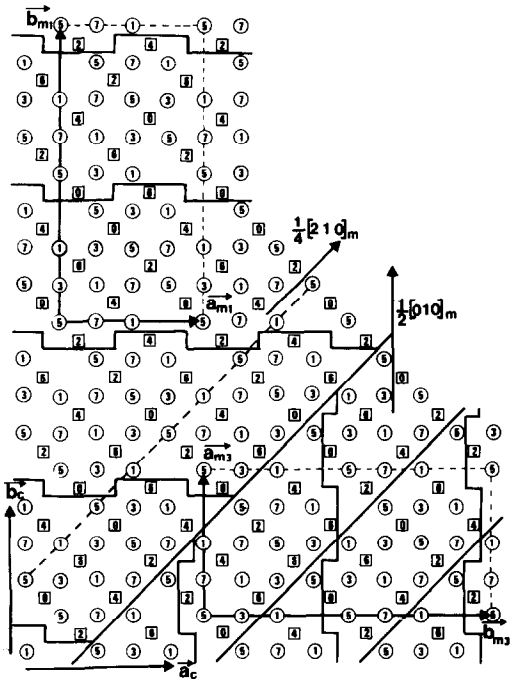

three twin zones of four coaxial variants that have a common binary axis. This clustering permits the strong shear strain of each variant to be canceled.

The orientation and structure of boundaries between coaxial variants are shown to be consistent with a good matching of the distorted oxygen array. Two kinds of boundaries are observed. The first ones are mixed boundaries with a diamond mirror as symmetry operation. They exhibit triple junctions with antiphase boundaries. The second ones, which are incoherent, are associated with planar faults parallel to the boundary plane. Regions with a high den-

FIG. 8. Structural model of a $(1\bar{2}0)_m$ twin boundary. The 3 twin variant is built with periodic $(1\bar{2}0)_m$ planar faults. $(001)_m$ projection of cation sites. Cation heights are given as multiples of $c_m/8$. Octahedral sites (○), tetrahedral sites (□).

sity of faults are frequently observed. The cation distribution in these regions can be interpreted as an intermediate cation order between those of the two twin variants. The eight translation variants which have been observed are the only ones which have a relatively low boundary energy. Twin and translation boundaries in each twin zone modify the PAPB repartition, and leave unchanged the cation distribution on spinel domain of the B structure.

References

1. P. Bassoul and J. C. Gilles, *J. Solid State Chem.* **58,** 383 (1985).
2. P. Bassoul, A. Lefebvre, and J. C. Gilles, *Mater. Res. Bull.* **11,** 11 (1976).
3. P. Bassoul, A. Lefebvre, and J. C. Gilles, *J. Phys. C* **7,** 80 (1977).
4. P. Bassoul, A. Dubon, A. Lefebvre, and J. C. Gilles, *Phys. Status Solidi A* **34,** 125 (1976).
5. R. Famery, P. Bassoul, F. Queyroux, C. Delamarre, and J. C. Gilles, *Phil. Mag. A* **45,** 63 (1982).
6. J. W. Christian, "Transformation in Metal and Alloy," Part I, Chap. 2, Permagon, Elmsford, N.Y. (1975).
7. B. Van Tendeloo, R. Wolf, and S. Amelinckx, *Phys. Status Solidi A* **40,** 531 (1977).
8. S. Amelinckx, R. Gevers, and J. Van Landuyt, "Diffraction and Imaging Techniques in Material Sciences," Vol. 1, p. 107, North-Holland, Amsterdam (1978).
9. A. Guinier, "Théorie et Technique de la Radiocristallographie," Chap. 13, Dunod, Paris (1964).
10. R. Portier and D. Gratias, *J. Phys. C* **4,** 17 (1982).
11. C. Boulesteix and B. Yangui, *Phys. Status Solidi A* **70,** 597 (1982).